FBG-based Shape Sensing Tubes for Continuum Robots

Seok Chang Ryu, *Member, IEEE* and Pierre E. Dupont, *Fellow, IEEE*

Abstract— Fiber Bragg gratings (FBG)-based optical sensors are a promising real-time technique for sensing the 3D curvature of continuum robots. Existing implementations, however, have relied on embedding optical fibers in small-diameter metal wires or needles. This paper proposes polymer tubes as an alternative substrate for the fibers. This approach separates the sensors from the robot structural components while using a minimal amount of the robot's tool lumen and providing the potential of inexpensive fabrication. Since the fibers are stiffer than the polymer substrate, however, design challenges arise in modeling strain transfer between the fibers and the tube substrate. To investigate the potential of this approach, a strain transfer model is derived and validated through simulation and experiment.

I. INTRODUCTION

Continuum robots take the shape of three dimensional curves and are able to change their shape through a combination of bending, rotation and extension or contraction of their structural components. Because of these capabilities, continuum robots are ideally suited for applications such as minimally invasive surgery. Their flexibility, however, leads to uncertainty in the shape of their backbone curve as well as in the location of their tip.

Approaches to real-time sensing that have been studied include imaging, electromagnetic (EM) tracking and force sensing for tendon-based actuation. These techniques all have shortcomings, however. For example, drawbacks with imaging include limited resolution (ultrasound), risk of ionizing radiation (x-ray or CT), and slow speed (MRI). Tendon length-based shape estimation is limited to single bends and its accuracy depends highly on the robot kinematic model.

In contrast to these approaches, a real-time sensing technology that could be easily inserted and removed from the robot is preferred because of its direct measurement, instant adaptability to the continuous shape change and ease of replaceability. Curvature sensing using fiber Bragg gratings (FBG) has received recent attention, due to its small size, biocompatibility and high sensitivity. Compared to EM sensors [1], FBG-based sensors are smaller, immune to EM noise and can contain multiple sensors along the length of a fiber. For example designs using attached [2] or embedded [3], [4] fibers have been implemented on 1mm diameter metal wires. Both approaches reasonably assumed a perfect strain transfer from the wire to FBG. While the small wire diameter had minimal effect on structural stiffness and made it possible to accommodate large curvatures (gratings

Seok Chang Ryu and Pierre Dupont are with the Department of Cardiovascular Surgery, Boston Children's Hospital, Harvard Medical School, Boston, MA 02115, USA `seokchang.ryu, pierre.dupont@childrens.harvard.edu`
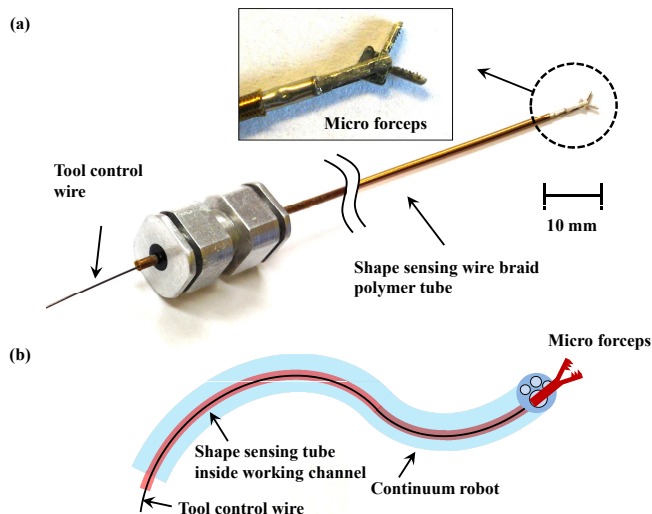
Fig. 1. Use example of a shape sensing tube: (a) incorporated shape-sensing capability in the wire braid polymer actuation tube of 1mm diameter forceps, (b) shape sensing and tool actuation tube inserted into a continuum robot.

can tolerate 0.8% strain [5]), a solid wire sensor running through the center of a robot's lumen can interfere with the insertion, removal and control of tip-mounted tools.

An alternative approach is to employ a tubular substrate made of a low modulus material. Such a design would use a minimal amount of the robot lumen and, despite a larger diameter, its compliance in bending would tend not to change the curvature of the robot into which it is inserted. An additional benefit of a compliant substrate is the strain reduction experienced by embedded optical fibers [6]. Using this effect, a sensing tube can be designed to experience larger bending strains than the optical fibers could otherwise tolerate.

A potential problem of a low-modulus homogeneous tubular substrate, however, is that compliance in bending is accompanied by compliance in torsion. Thus, any twisting of the sensing tube, arising either from sensor insertion or from robot motion, would confound robot shape estimation since the orientation of the sensors with respect to the cross section would be unknown. This issue has been recognized in the literature [7] and has been addressed using fiber optic torsion sensing, although this has been limited to large diameter devices due to the minimum fiber bending radius [8], [9]. Twisted-core fibers have also been developed (http://lunainc.com/), which sense bending and twisting simultaneously.

An inexpensive alternative solution is to employ a composite material substrate that is compliant in bending and stiff in
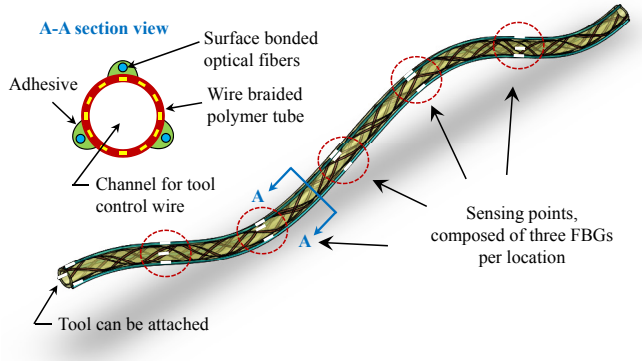
Fig. 2. Schematic of wire braided polymer tube with surface mounted optical fibers.

Fig. 3. Cross sectional sensor configuration with three fiber Bragg gratings. Dimensions correspond to prototype of section IV.

torsion. Such tubular elements are commonly used in medical devices, e.g., catheters and are composed of biocompatible polymer with an embedded wire braid. With a high braid angle, torsional rigidity is high while flexural stiffness remains low compared to that of the wire material [10]. Ovalization and the resultant buckling are another concern in polymer tube bending [11], but the resistance against it, called kink resistance, is also increased with a high braid angle [12]. As a result, the circular tube cross section is maintained even at high curvature, facilitating sensor modeling. Finally, a metal wire braid can be expected to reduce viscoelasticity in the polymer substrate.

An additional benefit of such a sensing tube is that it can be integrated with various tools or device delivery systems and not take up any additional area of the robot lumen. For example, Fig. 1 (a) depicts 1mm diameter forceps that our group uses with our concentric tube continuum robots. The forceps are controlled by relative translation between a wire-braided polymer tube and a wire running through the tube. This shape-sensing and tool-actuation tube occupies a single working channel and conforms to the continuum robot shape (Fig. 1 (b)).

The contribution of this paper is to develop and validate a mechanics-based model for these sensing systems so as to identify the important design variables. Section II presents the sensor design and reviews the related mechanics literature. A model describing strain transfer between the composite tube and the optical fibers is derived in section III and analyzed through simulation. Experimental results using a sensor prototype are provided in section IV and conclusions appear in section V.

II. SENSOR DESIGN

As shown in Fig. 2, the design considered here utilizes three surface mounted optical fibers. Although not considered here, an alternative design could embed the fibers in the tube cross section. Multiple sensing locations, distributed along the tube, are used to estimate the bending curvature at discrete values of arc length. From these values, the shape of the backbone curve can be reconstructed as in [13].

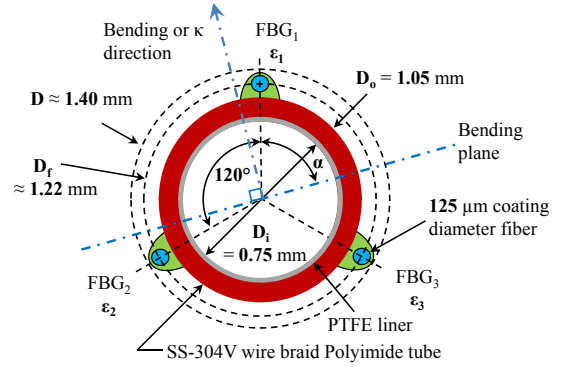Fig. 3 shows the detailed cross section at one sensing location. It is composed of three equally spaced optical fibers. To provide a sense of scale, the dimensions of the prototype considered later in the paper are provided here. The tube, composed of wire-braided (SS-304V) polymer, has an outer diameter of 1.05mm and an inner diameter of 0.75mm. The optical fibers have 125μm and 80μm coating and cladding diameters.

A. Curvature-Strain Model

Shape estimation starts from the local curvature calculation using the measured fiber strains. In [4], a simple linear model was used to relate fiber strain and the curvature based on beam mechanics, but the coefficients were calibration-based rather than model-based. Thermal strains were compensated in the same way. Improved linear curvature-strain models providing better understanding of the mechanics were developed in [2], [13], in which the coefficient was the fiber distance from the neutral axis. Also thermal strains were included in the analytical model and compensated by assuming uniformity of the cross section.

In contrast, the composite polymer substrate presents two complicating factors owing to its susceptibility to axial loading and its non-unity strain transfer ratio. These phenomena were negligible for prior metal wire sensors because of their high elastic modulus. These factors can be incorporated into the model of [13] by introducing the strain transfer ratio from the tube surface to the fiber, η, and the axial strain, ε_a, as

$$
\begin{aligned}
\varepsilon_1 &= \eta \cdot \{\varepsilon_{max} \cdot \sin(\alpha) + \varepsilon_a\} + \varepsilon_t \\
\varepsilon_2 &= \eta \cdot \{\varepsilon_{max} \cdot \sin(\alpha + 120^\circ) + \varepsilon_a\} + \varepsilon_t \qquad (1) \\
\varepsilon_3 &= \eta \cdot \{\varepsilon_{max} \cdot \sin(\alpha + 240^\circ) + \varepsilon_a\} + \varepsilon_t
\end{aligned}
$$

where ε_{max}, α and ε_t are the maximum bending strain in the tube, the angle of FBG_1 from the bending plane and thermal strain, respectively.

In Eq. 1, η is only applied to the mechanically induced strains, which is reasonable by assuming negligible thermal expansion, because thermal strain is not an actual strain, but temperature-induced changes in optical properties like the refractive index of gratings [14]. Also ε_t and ε_a are assumed uniformly distributed on the cross section.

Then, because of the equally spaced fiber arrangement, the combined uniform strain is calculated, independent of α, as

$$\varepsilon_{uni} = \varepsilon_t + \eta \cdot \varepsilon_a = \frac{\varepsilon_1 + \varepsilon_2 + \varepsilon_3}{3} \quad (2)$$

Solving Eq. 1 about α and ε_{max} using Eq. 2, yields,

$$\alpha = \arctan\{\frac{\sqrt{3} \cdot (\varepsilon_1 - \varepsilon_{uni})}{\varepsilon_2 - \varepsilon_3}\} \quad (3)$$

$$\varepsilon_{max} = \frac{1}{\eta} \cdot sgn\{(\varepsilon_1 - \varepsilon_{uni}) \cdot \sin\alpha\} \cdot \sqrt{\frac{2}{3} \sum_{i=1}^{3}(\varepsilon_i - \varepsilon_{uni})^2} \quad (4)$$

$$= \kappa \cdot \frac{D_o}{2} \quad (5)$$

where κ is tube curvature and D_o is used instead of fiber distance D_f, as opposed to [13], because of the definition of η. Compared to perfect strain transfer with $\eta = 1$, the sensing tube can undergo up to $\frac{1}{\eta} \geq 1$ times larger curvature for a given tensile strength of FBG and sensor size.

In order to solve for the magnitude of curvature, κ, using Eq. 4 and Eq. 5, the value of η is needed. Although a simple calibration technique could be used to estimate its value for a particular sensor, a mechanics-based model will provide design insights into the most important variables relating to its value. In this way, it can be possible to select design parameters to trade off maximum curvature versus sensitivity to meet desired performance specifications.

B. Strain Transfer Reduction Effects

As shown in Fig. 4 (b), $\eta < 1$ is caused by two strain reduction effects: the shearing effect in the soft interlayer and the fiber reinforcement effect on the low modulus substrate.

The first is related to the shear deformation in the adhesive and in the fiber coating. This effect has been studied using shear-lag models for embedded fibers [6], assuming that the layers only carry pure shear stress when they (at most, a few GPa) are much softer than the silica glass (72 GPa) used for the fiber core and cladding. Although this shear-lag model does not consider transverse shear stress causing bending deformation, the insensitivity of the FBG to this stress allows its reasonable use for sensing tube bending.

For surface bonded fibers, a modified shear-lag model was developed in which the component of η due to shear lag, η_{SL}, is dominated by the fiber bonding length and the bottom adhesive thickness while insensitive to the side or top adhesive [15]. This analytical model, however, assumed an unrealistic axisymmetry for the adhesive. In [16], this axisymmetry was discarded, however, a simplified model geometry was assumed in which the substrate had a significantly larger cross section than the fiber, an assumption unsuitable for thin polymer tubes.

In addition, these shear-lag models in fibers assume a uniform strain applied to the long bonded fibers [15] or require the strain profile in order to obtain the fiber strain [16], which is not feasible for a sensing tube experiencing a tortuous curve along a fixed fiber length.
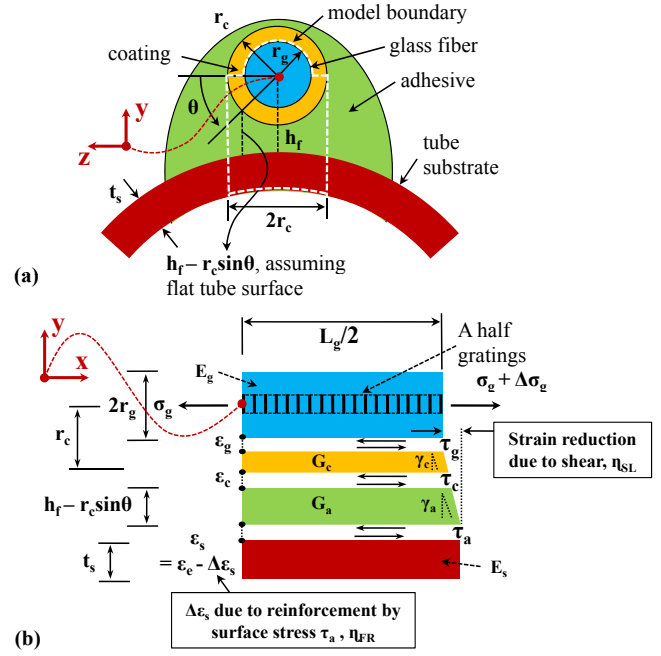

Fig. 4. Schematic for modeling strain reduction in a surface bonded fiber (refer to Table. I for variables). (a) Cross sectional view, (b) Side view for half the length of an FBG sensor.

The second strain reduction effect is due to the high modulus glass fibers acting as reinforcing elements for the soft substrate. The resulting bending strain experienced by the substrate is reduced by $\Delta\varepsilon_s$ from the expected strain without fibers, ε_e. This reinforcement effect on a low modulus substrate has been studied in both surface bonded and embedded strain gauges [17], where the interfacial surface shear stress was transferred into the normal stress in a semi-infinite substrate.

For fiber optic sensors with a relatively long bonding length, the η due to the fiber reinforcement effect, η_{FR}, was obtained using simple composite theory [16], which is, however, based on an assumption of equivalent strains for all components. Values of η estimated with this model were consistently less than the experimental results, though the causes were not discussed.

These works do provide, however, a starting point for developing a strain transfer model for the proposed sensing tube as derived in the next section. Following [15], both top and side adhesives can be neglected. An analytical model for a surface bonded fiber can then be formulated assuming a circular glass fiber with a bottom half soft coating, a bottom adhesive layer and a relatively flat polymer tube substrate (the white-dashed region in Fig. 4 (a)). Using symmetry, half the length of an FBG sensor can be considered (Fig. 4 (b)).

III. STRAIN TRANSFER MODEL

The strain transfer model is comprised of an interfacial shear model and a fiber reinforcement model. For modeling shear lag, axisymmetry is only applied within the thin fiber coating and the circular geometry between the coating and

r_g	radius of fiber glass core and cladding layers
r_c	radius of fiber coating layer
L_g	length of fiber Bragg grating
t_s	thickness of thin tube substrate
h_f	fiber distance from tube surface
θ	angle from horizontal axis
E_g	Young's modulus of fiber core and cladding
E_s	Young's modulus of thin tube substrate
G_c	shear modulus of fiber coating layer
G_a	shear modulus of adhesive layer
γ_c	shear strain in fiber coating layer
γ_a	shear strain in adhesive layer
u_g	displacement at fiber cladding and coating interface
u_c	displacement at fiber coating and adhesive interface
u_s	displacement at adhesive and tube interface
ε_g	normal strain of fiber core and cladding
ε_c	normal strain at fiber coating and adhesive interface
ε_s	normal strain at adhesive and tube interface
ε_e	expected normal strain at tube surface without fiber
σ_g	normal stress of fiber core and cladding
τ_g	shear stress at fiber cladding and coating interface
τ_c	shear stress in fiber coating layer
τ_a	shear stress in adhesive layer
η	strain transfer ratio from substrate to fiber
η_{SL}	η due to shear lag effect
η_{FR}	η due to fiber reinforcement effect
α	shear lag parameter
β	fiber reinforcement parameter

adhesive is considered. On the other hand, for the reinforcement effect, the surface shear stress at the adhesive-tube interface, τ_a obtained from the shear-lag based model, is assumed to create $\Delta\varepsilon_s$ on the surface, which allows the possibility of a strain difference between components, in contrast to [16]. Each model is described below. All variables are summarized in Table. I.

A. Interfacial Shear Effect

From the force equilibrium for each layer in Fig. 4 (b), the following equations are obtained for the glass fiber (core and cladding), the coating and the adhesive,

$$\int_0^\pi \tau_g(r_g,\theta,x) \cdot r_g d\theta = \Delta\sigma_g \cdot \pi r_g{}^2 = E_s\varepsilon_g \cdot \pi r_g{}^2 \quad (6)$$

$$\int_0^\pi \tau_c(r,\theta,x) \cdot r d\theta = \int_0^\pi \tau_g(r_g,\theta,x) \cdot r_g d\theta \quad (7)$$

$$\int_{-r_c}^{r_c} \tau_a(x,-h_f,z)dz = \int_0^\pi \tau_c(r_c,\theta,x) \cdot r_c d\theta \quad (8)$$

where σ, τ and r are normal stress, shear stress and radius, respectively (subscripts g, c and a indicate glass core, coating and adhesive.). ε_g is the glass fiber strain, measured by the FBG.

From Eq. 7 and the assumed axisymmetry within the bottom half of the coating layer, the shear stress in the coating, at radial distance r, is written as,

$$\tau_c(r,\theta,x) = \frac{r_c}{r}\tau_c(r_c,\theta,x) \text{ for } r_g \leq r \leq r_c \quad (9)$$

Using Eq. 9 and the assumption of linear elasticity and pure shear strain transfer in the soft layers, we also obtain

the following relationships for the two interlayers,

$$u_c(x) - u_g(x) = \int_{r_g}^{r_c} \gamma_c(r,\theta,x)dr \quad (10)$$

$$= \frac{r_c}{G_c}\tau_c(r_c,\theta,x) \cdot \ln\frac{r_c}{r_g} \quad (11)$$

$$u_s(x) - u_c(x) = (h_f - r_c\sin\theta)\gamma_a(r_c,\theta,x) \quad (12)$$

$$= (h_f - r_c\sin\theta)\frac{\tau_a(r_c,\theta,x)}{G_a} \quad (13)$$

where u, γ, G and h_f are displacement at interfaces, shear strain, shear modulus and fiber distance from the outer surface of substrate (subscript s indicates substrate.).

Combining Eq. 11 with Eq. 13, the shear stress of the adhesive at the interface with the coating, $\tau_a(\theta,x)$, is obtained. Because this stress should be equivalent with that of the coating at the interface, which can be calculated using Eq. 9 at $r = r_c$, the interfacial shear stress at coating, $\tau_c(r_c,\theta,x)$ is expressed as,

$$\tau_c(r_c,\theta,x) = \tau_a(r_c,\theta,x) = \frac{u_s(x) - u_g(x)}{\frac{(h_f - r_c\sin\theta)}{G_a} + \frac{r_c}{G_c}\ln(\frac{r_c}{r_g})} \quad (14)$$

which is linearly proportional to the displacement of the fiber with respect to the substrate. In the denominator of Eq. 14, the first term is related to the shear of the adhesive layer while the second term is related to the axisymmetric shear within the bottom half of the coating layer.

Assuming uniform strains in the $L_g/2$ half length of the FBG, reasonable with fiber bonding length exceeding 11 mm [18], the displacements are replaced with $u_g(x) = L_g/2 \cdot \varepsilon_g$, $u_c(x) = L_g/2 \cdot \varepsilon_c$ and $u_s(x) = L_g/2 \cdot \varepsilon_s$. Then, the η due to the shear-lag effect, η_{SL}, is defined as the constant ratio of ε_g to ε_s.

Based on these assumption, substituting Eq. 14 into Eq. 7, then again into Eq. 6, η_{SL} is obtained as,

$$\eta_{SL} = \frac{\varepsilon_g}{\varepsilon_s} = \frac{\alpha}{1+\alpha} \quad (15)$$

where the shear parameter α is

$$\alpha = \frac{L_g}{2\pi r_g{}^2 E_g}\int_0^\pi \frac{1}{\frac{(h_f - r_c\sin\theta)}{G_a} + \frac{r_c}{G_c}\ln(\frac{r_c}{r_g})}d\theta \quad (16)$$

which contains both mechanical and geometrical properties of the soft interlayers.

Due to the positive α, η_{SL} is always less than unity, but for a significantly large value of α, caused by either harder interlayers or a thin bottom adhesive, η_{SL} approaches 1.

B. Fiber Reinforcement Effect

To calculate the fiber reinforcement effect, τ_a at the tube surface is replaced with an uniform normal stress on the thin substrate piece under the gratings. Then, substituting Eq. 14 into Eq. 8 and adopting Eq. 15, the strain reduction, $\Delta\varepsilon_s$, is
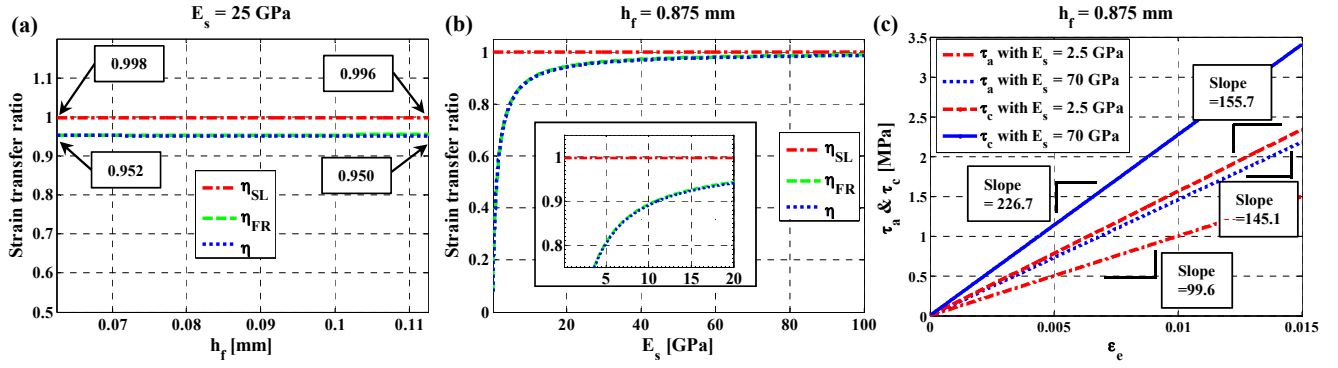
Fig. 5. Strain transfer reduction model simulation : (a) η with different adhesive thickness, (b) η with different substrate modulus, (c) maximum τ_a and τ_c with varying ε_e

TABLE II

MATERIAL PROPERTY AND MODEL GEOMETRY FOR SIMULATION

$r_g[mm]$	$r_c[mm]$	$h_f{}^1[mm]$	$t_s[mm]$	$L_g[mm]$
0.04	0.0625	0.0625−0.1125	0.15	5
$E_g[GPa]$	$G_c{}^2[GPa]$	$G_a{}^3[GPa]$	$E_s[GPa]$	
72.0	0.933	1.379	0.1−100.0	

obtained with the following relationship,

$$\Delta\varepsilon_s = \frac{1}{2r_c E_s t_s}\int_{-r_c}^{r_c}\tau_a(z,x)dz \tag{17}$$

$$= \frac{1}{2E_s t_s}\int_0^\pi \tau_c(r_c,\theta,x)d\theta \tag{18}$$

$$= \beta\varepsilon_s \tag{19}$$

where the reinforcement parameter β is

$$\beta = \frac{L_g(1-\eta_{SL})}{4E_s t_s}\int_0^\pi \frac{1}{\frac{(h_f - r_c\sin\theta)}{G_a} + \frac{r_c}{G_c}\ln(\frac{r_c}{r_g})}d\theta \tag{20}$$

Using superposition, ε_s is the sum of ε_e with $-\Delta\varepsilon_s$, that is,

$$\varepsilon_s = \varepsilon_e - \Delta\varepsilon_s = \varepsilon_e - \beta\varepsilon_s \tag{21}$$

Thus, η_{FR} is written as,

$$\eta_{FR} = \frac{\varepsilon_s}{\varepsilon_e} = \frac{1}{1+\beta} \tag{22}$$

When the E_s or t_s is sufficiently large, β becomes negligible, resulting in approximately unity η_{FR}.

Combining Eq. 22 with Eq. 15 yields the relationship of ε_g with ε_e as

$$\varepsilon_g = \eta_{SL} \cdot \eta_{FR} \cdot \varepsilon_e = \eta \cdot \varepsilon_e \tag{23}$$

For the case of bending strain only in FBG_1 (Fig. 3), $\varepsilon_e = \kappa \cdot \sin\alpha \cdot \frac{D_o}{2} = \varepsilon_{max} \cdot \sin\alpha$.

[1]the available range acquired from the sensor dimension
[2]estimated from the properties of Polyimide with 2.5 GPa of Young's modulus and 0.34 of Poisson's ratio
[3]$http://www.henkelna.com/$

C. Simulation

To demonstrate the value of the model, the effects of adhesive thickness, i.e., $h_f - r_c$, and E_s on η are studied. In addition, interfacial shear stress is estimated for different values of ε_e. The mechanical and geometrical properties used for the simulation are summarized in Table. II.

As shown in Fig. 5 (a) and (b), η_{SL} is approximately unity in the given dimension, because the thin adhesive layer results in a large α (Eq. 15), such that E_s has a dominant effect on η. Thus, in this dimension, it is reasonable to assume the same η for all fibers as in Eq. 1, regardless of the adhesive amount. In each FBG, however, non-uniform adhesive along the gratings can distort the spectral peak so care should be taken to distribute adhesive evenly along the length of each set of gratings.

A substrate with a modulus higher than 10 GPa transfers more than 90% of its strain. Thus, in this range, low sensitivity is not a concern. Instead, when larger curvature measurements are required in a given sensor size, tube modulus should be modified rather than changing the adhesives. According to [10], low modulus is obtainable by further increasing the braid angle, by using a softer polymer, or by using different wire materials such as Kevlar 49 fibers (112 GPa). For such softer sensors, differential sensing using four orthogonally arranged fibers as in [2] can be adopted if necessary to double the sensitivity, though it increases its flexural rigidity as well as the cost.

It can also be seen that maximum τ_a and τ_c at $\theta = \pi/2$, tend to be slightly reduced for a softer substrate, probably due to the buffering effect (Fig. 5 (c)). They are expected to be less than 5 MPa at both interfaces. The slopes of τ increase in proportion to $(1-\eta_{SL})\eta_{FR}$ as expected from Eq. 14, 15 and 22.

This enables the use of a low shear strength (3-20 MPa depending on adherence) super glue instead of a higher-viscosity epoxy, the latter being more difficult for micro-scale fabrication. However, at larger diameters, epoxy is effective when high strain transfer is necessary.
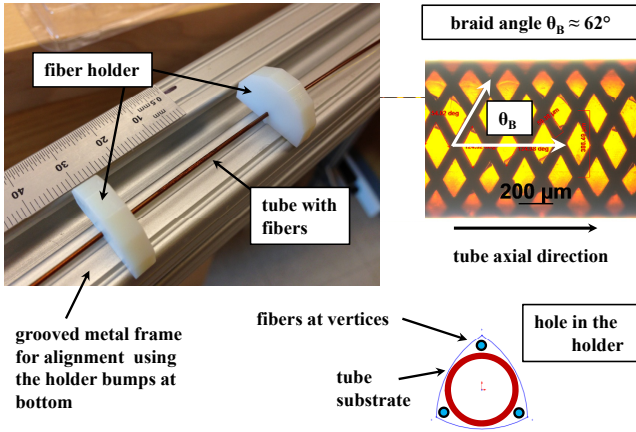
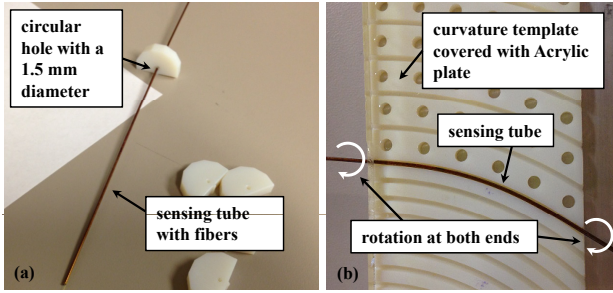Fig. 6. Surface bonding process for optical fibers on a wire braid polymer tube.

Fig. 7. Sensing tube calibration. (a) Prototype using three optical fibers, (b) Calibration process using curvature templates.

Fig. 8. Sensor calibration results. (a) ε_e versus compensated ε_g, (b) Curvature error produced by tensile, compressive and mean values of η.

IV. EXPERIMENTS

A low-cost sensor prototype was constructed using one FBG fiber and two identical fibers without FBGs (Fig. 6) to investigate the effect of the soft substrate on the curvature estimation in single-plane bending. A 3D-printed fiber holder with a curved triangular hole holds the fibers (Technica SA, Switzerland) and a wire braided Polyimide tube with a braid angle of $62°$ (295-VI, MicroLumen, USA). The longitudinal Young's modulus of the tube was measured as around 24.79 GPa, with an expected $\eta \approx 0.951$.

Based on Sec. III-C, a medical device super glue (Loctite 4013, Henkel, USA) was applied to slightly tensioned straight fibers. After curing, excess glue was carefully removed using Acetone, to reduce flexural rigidity and size. As shown in Fig. 7 (a), the prototype smoothly passes through a 1.5mm circular hole so that $D \approx 1.4$mm since its minimum, $D_o + 4r_c$, is 1.3mm. In this dimension, the effect of non-uniform adhesive thickness on η, an expected manufacturing error, is negligible as anticipated in Sec. III-C. This was also supported by the sensor's sharp spectral peak for all curvatures, indicating sufficiently uniform adhesive along the gratings

A. Calibration and Shape Sensing Capability

The sensor prototype was manually rotated 2π within grooves of a curvature template covered with a transparent acrylic plate (Fig. 7 (b)) and sensor signal was recorded
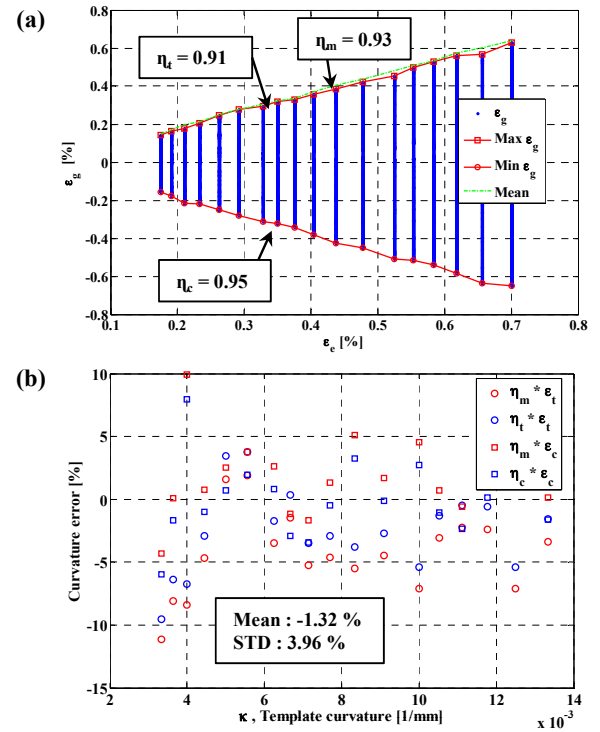
with an optical interrogator at 1 kHz (sm130, Micron Optics, USA). In the process, the clearance between the grooves and the sensing tube, necessary for the smooth rotation, can cause calibration error.

As shown in Fig. 8 (a), for each groove with a fixed curvature, all ε_g, after axial and thermal strain compensation, are plotted on a vertical line. The maximum and minimum values in each line correspond to the maximum tension and compression at the given curvature.

Although the results exhibit fair linearity and symmetry in tension and compression, the η obtained from the linear fit of each set of the maxima (ε_t) and the minima (ε_c) is slightly different from each other, i.e., 0.91 (η_t) and 0.95 (η_c), respectively. The mean (η_m) is given by 0.93. While these values are close to the expected value of 0.951, the variation is large enough to produce significant error in curvature as shown in Fig. 8 (b).

To investigate the effect of curvature error on robot tip position error, P_{err}, and tip orientation error, O_{err}, a robot of constant curvature and length 80mm is assumed. This length corresponds to the actively controlled portion of a continuum robot used for intracardiac surgery [19]). At each curvature, the FBG can measure strain either in tension or in compression. Both cases acquired from the calibration were considered, but the constant η_m was used in curvature estimation. The resulting tip errors are plotted in Fig. 9. These are given by P_{err}=0.84±0.62 mm (96.7% less than 2 mm error) and O_{err}=1.21±0.91° (80.7% less than 2° error).
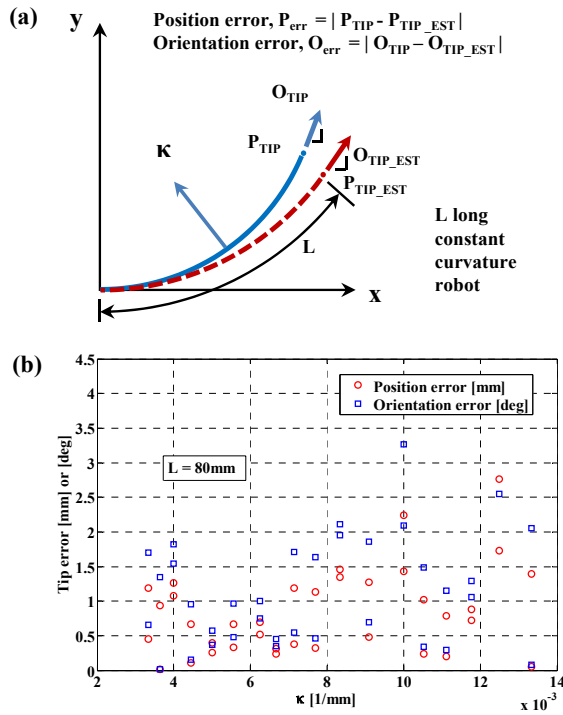
Although the required sensor accuracy depends on ap-

Fig. 9. Estimated position and angle error for an 80mm long constant-curvature robot. (a) Error definition schematic, (b) Tip errors produced by the mean value of η.

plications, tip position errors of 1-2 mm and orientation errors of 0.5-2° are considered sufficient in most present minimally invasive surgical applications [20]. In addition, the other errors from the registration and organ or patient movements are often much larger, so sensor improvement over the requirements has little effect on the system accuracy.

Therefore, while these tip errors can likely be reduced through improved fabrication and calibration processes, they indicate that the proposed approach holds promise.

V. CONCLUSIONS

The proposed composite tubular shape sensor provides sufficient torsional rigidity and flexural compliance through the use of wire braid reinforcement. Additionally, this design provides a spacious tool channel. As a first step toward developing this concept, a mechanics-based model has been derived to characterize the strain transfer between the compliant tube and the stiff glass fibers. This model incorporated both the shear lag as well as the fiber reinforcement effects and provides a means to identify the important design variables. This approach was illustrated through model simulation and a simple prototype was presented to validate the model. In current research, manufacturing tolerances and calibration procedures are being improved to improve sensor accuracy.

REFERENCES

[1] H. Sadjadi, K. Hashtrudi-Zaad, and G. Fichtinger, "Fusion of electro-magnetic trackers to improve needle deflection estimation: Simulation study," *Biomedical Engineering, IEEE Transactions on*, vol. 60, no. 10, pp. 2706–2715, Oct 2013.

[2] J. Yi, X. Zhu, H. Zhang, L. Shen, and X. Qiao, "Spatial shape reconstruction using orthogonal fiber Bragg grating sensor array," *Mechatronics*, vol. 22, pp. 679–687, 2012.

[3] R. Roesthuis, S. Janssen, and S. Misra, "On Using an Array of Fiber Bragg Grating Sensors for Closed-Loop Control of Flexible Minimally Invasive Surgical Instruments," *IEEE/RSJ International Conference on Intelligent Robots and Systems (IROS)*, November 2013.

[4] Y.-L. Park, S. Elayaperumal, B. Daniel, S. Ryu, M. Shin, J. Savall, R. Black, B. Moslehi, and M. Cutkosky, "Real-Time Estimation of 3-D Needle Shape and Deflection for MRI-Guided Interventions," *IEEE/ASME Transactions on Mechatronics*, vol. 15, no. 6, 2010.

[5] D.-H. Kang, S.-O. Park, C.-S. Hong, and C.-G. Kim, "Mechanical Strength Characteristics of Fiber Bragg Gratings Considering Fabrication Process and Reflectivity," *Journal of Intelligent Material Systems and Structures*, vol. 18, pp. 303–309, 2007.

[6] H.-N. Li, G.-D. Zhou, L. Ren, and D.-S. Li, "Strain Transfer Coefficient Analyses for Embedded Fiber Bragg Grating Sensors in Different Host Materials," *Journal of Engineering Mechanics*, vol. 135, pp. 1343–1353, 2009.

[7] J. Moore and M. Rogge, "Shape sensing using multi-core fiber optic cable and parametric curve solutions," *Optics Express*, vol. 20, no. 3, pp. 2967–2973, 2012.

[8] L. Kruger, P. Swart, and A. Chtcherbakov, "Non-contact torsion sensor using fibre Bragg gratings," *Measurement Science and Technology*, vol. 15, pp. 1448–1452, 2004.

[9] M. Konings, T. van Leeuwen, W. T. M. Mali, and M. Viergever, "Torsion measurement of catheters using polarized light in a single glass fibre," *Physics in Medicine and Biology*, vol. 43, pp. 1049–1057, 1998.

[10] J. Carey, A. Fahim, and M. Munro, "Design of Braided Composite Cardiovascular Catheters Based on Required Axial, Flexural, and Torsional Rigidities," *Journal of Biomedical Materials Research*, vol. 70, pp. 73–81, 2004.

[11] M. Wadee, M. Wadee, A. Bassom, and A. Aigner, "Longitudinally inhomogeneous deformation patterns in isotropic tubes under pure bending," *Proc. of the Royal Society A: Mathematical, Physical and Engineering Sciences*, vol. 462, pp. 817–838, 2005.

[12] H. Zhang, P. Zhou, and R. He, "Effect of Braid Angle on the Flexural Kink Resistance of Braided Metal Wire-Reinforced Polymer Composite," *SEM Annual Conference and Exposition on Experimental and Applied Mechanics*, 2009.

[13] M. Abayazid, M. Kemp, and S. Misra, "3D Flexible Needle Steering in Soft-Tissue Phantoms using Fiber Bragg Grating Sensors," *IEEE International Conference on Robotics and Automation (ICRA)*, May 2013.

[14] K. Hill and G. Meltz, "Fiber Bragg Grating Technology Fundamentals and Overview," *Journal of Lightwave Technology*, vol. 15, no. 8, pp. 1263–1276, 1997.

[15] K. Wan, C. Leung, and N. Olson, "Investigation of the strain transfer for surface-attached optical fiber strain sensors," *Smart Materials and Structures*, vol. 17, pp. 1263–1276, 2008.

[16] W. Li, C. Cheng, and Y. Lo, "Investigation of strain transmission of surface-bonded FBGs used as strain sensors," *Sensors and Actuators A: Physical*, vol. 149, pp. 201–207, 2009.

[17] A. Ajovalasit, S. Fragapane, and B. Zuccarello, "The Reinforcement Effect of Strain Gauges Embedded in Low Modulus Materials," *Strain*, vol. 49, pp. 366–376, 2013.

[18] S. Martin and J. Blackshire, "Effect of Adhesive Material Properties on Induced Stresses in Bonded Sensors," *AIP Conference Proceedings*, vol. 894, pp. 1524–1531, 2006.

[19] A. Gosline, N. V. Vasilyev, E. Butler, C. Folk, A. Cohen, R. Chen, N. Lang, P. J. del Nido, and P. E. Dupont, "Percutaneous intracardiac beating-heart surgery using metal MEMS tissue approximation tools," *The International Journal of Robotics Research*, vol. 31, no. 9, pp. 1081–1093, 2012.

[20] P. Gomes, *Medical Robotics: Minimally Invasive Surgery*, ser. Woodhead Publishing Series in Biomaterials. Elsevier Science, 2012.